Synthesis and characterization of rGO/Fe^0/Fe$_3$O$_4$/TiO$_2$ nanocomposite and application of photocatalytic process in the decomposition of penicillin G from aqueous

Jamal Mehralipour [a,b,c], Susan Bagheri [a,b], Mitra Gholami [a,b,*]

[a] Research Center for Environmental Health Technology, Iran University of Medical Sciences, Tehran, Iran
[b] Department of Environmental Health Engineering, School of Public Health, Iran University of Medical Sciences, Tehran, Iran
[c] Student Research Committee, Iran University of Medical Sciences, Tehran, Iran

ARTICLE INFO

ABSTRACT

In this study, we synthesized rGO/Fe^0/Fe$_3$O$_4$/TiO$_2$ nanocomposite according to Hummer's, and straightforward sol-gel method. The FESEM, EDX, TEM, FT-IR, XRD, BET, UV spectra, and VSM analysis were applied to determine the catalyst properties. Optimization of influence parameters on photocatalytic process performance to penicillin G degradation in aqueous media. pH (4–8), nanocomposite dose (10–20 mg/L), reaction time (30–60 min), and penicillin G concentration (50–100 mg/L) were optimized via central composite design. In the optimum condition of PCP, supplementary studies were done. As a result of the analysis, the nanocomposite was well synthesized and displayed superior photocatalytic properties for degrading organic pollutants. In addition to being magnetically separable, the synthesized rGO/Fe^0/Fe$_3$O$_4$/TiO$_2$ nanocomposite exhibits high recyclability up to 5 times. The quadratic model of optimization is based on the adjusted R^2(0.99), and predicated R^2(0.97) suggested. According to the analysis of variance test, the model was significant (F-Value = 162.95, P-Value = 0.0001). Photocatalytic process is most efficiently decomposed at pH = 6.5, catalyst dose = 18.5 mg/L, reaction time = 59.1 min, and penicillin G concentration = 52 mg/L (efficiency = 96%). The chemical oxygen demand and total organic carbon decrease were 78, and 65%. The photolysis and adsorption mechanism as a single mechanism had lower performance in penicillin G degradation. Benzocaine had the greatest effect on reducing the efficiency of the process as a radical scavenger. The $^\circ$OH, h^{+} and O$_2^{\bullet-}$ were the main reactive oxidant species in penicillin G removal. Phenoxyacetaldehyde, Acetanilide, Diacetamate, Phenylalanylglycine, N-Acetyl-L-phenylalanine, Diformyldapsone, and Succisulfone were the main intermediates in penicillin G degradation. The results indicated the photocatalytic process with rGO/Fe^0/Fe$_3$O$_4$/TiO$_2$ nanocomposite on a laboratory scale has good efficiency in removing penicillin G antibiotic. The application of real media requires further studies.

1. Introduction

Due to its resistant organic compounds (ROCs), high use, and sustainability, industrial wastewater, such as pharmaceutical wastewater, has been considered a major water pollutant in recent decades [1,2]. Predictably, significant levels of antibiotics (as

parent compounds or metabolized compounds) will enter the environment from pharmaceutical, hospital, and animal husbandry wastewater since antibiotics are widely used in medicine, veterinary medicine, and aquaculture [3]. Because, Antibiotics cause human pathogenic bacteria, the development of metabolites and hazardous residues have received special attention from researchers. Some reports indicate that worldwide 10^5 to 20^6 tons of antibiotics are consumed each year [1,4,5]. There is no difference in the solubility order among antibiotics; water is more soluble than ethanol, and ethanol is more soluble than 2-propanol and acetone. In comparison to acetone, water has a three-orders-of-magnitude higher solubility [6]. One of the popular categories of antibiotics is the penicillin family. The structure of this family contains a lactam ring. Penicillin G ($C_{16}H_{17}N_2NaO_4S$, PNG) is one of the members of the penicillin family that is produced from the fungus called penicillium [7,8]. PNG is used to treat a wide range of diseases in humans, animals, and aquatic organisms [9]. Its mechanism of action involves the inhibition of the production of peptidoglycans, which destroys the bacterial cell wall. It is soluble in water (pKa = 2.75) and can destroy the cell wall of bacteria. In some countries, more than 12,000 tons of this antibiotic are produced annually. It has the highest antimicrobial activity among natural antibiotics [10]. The concentration of PNG in the environment have been reported in the range of ng to mg [11]. To date, several processes have been applied to the treatment of wastewater containing PNG at the lab and pilot scale, such as adsorption [12], catalytic ozonation process [13], electro-oxidation process [14], electro-Fenton process [15], membrane bioreactor [16], and photocatalytic process (PCP) [7]. As one of the most advanced oxidation processes (AOPs), PCP utilizes light energy (UV–C, UV-A, and visible light) in conjunction with a photocatalyst that consists of metal oxides (semiconductors) to provide degradation or mineralization of organic pollutants. Nowadays, PCP has attracted attention because of its facile process, stability, and ability to decompose organic structures like an antibiotic to non-hazardous byproducts, and inorganic compounds like H_2O and CO_2 [17]. The main drawback of classic photocatalysts such as TiO_2, and ZnO is the large gap band, which makes only UV-C can activate them. In addition to the potential dangers for humans, UV-C contains only 4% of the sun's waves, which limits the application of the PCP via classic photocatalysts. Today, researchers are looking to use new photocatalysts with short-band gaps that can be activated in UV-A and visible light [18]. In the field of purification, PCP is a modern, green, and promising technique. The photocatalyst converts light energy into chemical energy on the surface of the catalyst. When the photon energy exceeds/equals the band gap of the photocatalyst, electrons in the valence band move into the conduction band, and holes are generated in the conduction band. As a result of the excited electron-hole pairs, free radicals are produced directly or indirectly, which can cause organic compounds to decompose into inorganic compounds [19]. In the PCP, carrier separation and transfer are estimated to take approximately 10^{-12}-10^{-6} s, which is longer than the time required for the recombination of photogenerated electron-hole pairs, which take 10^{-12}-10^{-3} s. Increased carrier transfer rates are therefore one of the most effective strategies for enhancing photocatalytic efficiency [20]. In contrast to ZnO, SnO_2, ZrO_2, CdS, and other semiconductor materials that suffer from their own losses, TiO_2 is a popular photocatalyst because of its non-toxicity, low cost, excellent chemical stability, and outstanding corrosion resistance [21]. Despite this, it is extremely difficult for photo-generated electron-hole pairs to be recombined on TiO_2's surface when they are caused by light-excited electrons. Furthermore, TiO_2 is an inefficient photocatalyst due to a high aggregation rate, which limits its application to practical photocatalysis [22]. As a result, TiO_2 is usually modified with other materials in order to enhance its photocatalytic properties in order to overcome its lack of photocatalytic activity when used alone. The combination of graphene-based materials with TiO_2 appears to be a promising candidate since it can serve as a buffer against particle aggregation as well as facilitate the transfer of electron-hole pairs generated by photons [23]. As a result of its high surface area, low mass, high electrical conductivity, and a large number of functional groups, such as carboxyls, hydroxyls, and epoxy groups, graphene oxide (GO) is a very attractive compound because of its excellent properties [24,25]. However, after the photocatalyst process, the used TiO_2 is commonly recovered through tedious filtration or high-speed centrifugation in order to prevent secondary pollution in the source, which is highly inconvenient, not economically feasible, and difficult to operate. In light of this, magnetite particles have been increasingly used in lab-scale magnetic separations [26]. Additionally, TiO_2 combined with iron oxide family materials has been shown to be more effective in destroying organic pollutants. As an example, Xu et al. reported high performance photocatalytic recovery of Cr(VI) in TiO_2/FeO versus pour TiO_2 [27]. Alternatively, Ag, Pt, Pd, Ru, Rh, and Fe have been added to TiO_2 in order to prevent recombination of electron-hole pairs. As reported in previous studies, Fe^0 traps electrons produced by TiO_2 photocatalysis by the two half-reactions of Fe^{3+}/Fe^{2+} and Fe^{2+}/Fe^0, preventing electron-hole recombination [28]. Bibi et al. applied $rGO/Fe_3O_4/TiO_2$ in a photocatalytic process to degrade malachite green and methylene blue. According to this study, from 3.2 eV to 2.6 eV, the band gap decreased. For malachite green (MG) degradation, the photocatalyst process via $rGO/Fe_3O_4/TiO_2$ showed the photocatalytic process is commendable (99%) in comparison to pure TiO_2 (67%) under visible light in 55 min [29]. Based on the above explanations, the presence of pharmaceutical compounds, especially antibiotics, in aquatic environments has become an environmental problem, and the aim of this study is to synthesize the catalyst with high photocatalytic ability to degrade the antibiotic PNG from aquatic environments. Various analyzes were performed to measure the quality of the synthesized catalyst. And, the test design method has been used to reduce human error, reduce the number of test steps, and optimize the process. Photocatalysis process depend on several parameters. We applied to central composite design (CCD) to investigation of effect of parameters on performance, so, in this study, $rGO/Fe^0/Fe_3O_4/TiO_2$ nanocomposite was synthesized via hydrothermal method. To investigate the synthesized $rGO/Fe^0/Fe_3O_4/TiO_2$ nanocomposite, some spectroscopic and analytical techniques were used.

2. Material and methods

2.1. Analytical chemicals and reagents

The chemicals were purchased from Sigma-Aldrich and were not refined further. Ethanol (C_2H_5OH: 97%), methanol (CH_3OH: 98%), titanium (IV) butoxide [Ti(C_4H_9O)4: 98%], sulfuric acid (H_2SO_4: 95–97%), sodium hydroxide (NaOH: 99%), sodium nitrate

(NaNO$_3$: 98%), sodium borohydride (NaBH$_4$, 98%), graphite powder (99%), potassium permanganate (KMnO$_4$: 99%), hydrochloric acid (HCl: 37%), sodium sulfate (Na$_2$SO$_4$: 98%), Ammonium (NH$_4^+$: 99%), acetonitrile (C$_2$H$_3$N: 99%), ferric chloride (FeCl$_3$.6H$_2$O:97%), ferrous chloride (FeCl$_2$.4H$_2$O: 97%), PNG (C$_9$H$_{11}$N$_2$O$_4$S), with analytical grade bought. COD vial (Low range: 0–150 mg/L) bought from Laviband Co. Deionized water was used to prepare all solutions.

2.2. Preparation of nanocomposite

2.2.1. Preparation of rGO

We prepared graphene oxide according to a modified Hummers' method [30]. Briefly, it was prepared by mixing 10 g of graphite powder (GP) and 5 g of sodium nitrate in 230 mL of sulfuric acid in a flask and stirring the solution vigorously at an ice bath temperature (0 to 5 °C) for 60 min. Moreover, 30 g of potassium permanganate was gently added to the mixture and stirred continuously until green color developed and the temperature was maintained at 15 °C. As soon as the ice bath has been removed, stir the mixture at 35 °C for 24 h until the color of the mixture becomes light brown. It was added gradually to the suspension 460 mL of deionized water, and the reaction temperature increased to 98 °C, and a brownish color was observed. After adding 200 mL of warm water under stirring, H$_2$O$_2$ (10 mL) was added to terminate the reaction. To purify the solution, the pH of the solution was neutralized by adding 10% HCl and then washing with deionized water. This was followed by oven drying at 60 °C for 2 h. An ultrasonic bath was used to exfoliate 0.1 g of GO in 100 mL of water. The GO suspension was stirred at 50 °C for 12 h after adding 0.15 g of ascorbic acid. Lastly, the rGO was obtained. After washing with ethanol, centrifuging, and drying at 80 °C in a vacuum oven for 8 h, an rGO sample was obtained.

2.2.2. Preparation of rGO/Fe^0, and rGO/Fe^0/Fe$_3$O$_4$

As a starting point, 1.2 g of synthesized rGO was dissolved in 240 mL of distilled water in a round flask. Then, 60 mL of FeCl$_3$.6H$_2$O (1 M) was dissolved in a solution of rGO at 25 °C, and 140 mL of NaBH$_4$ (1.6 M) was added to the solution and stirred for 2 h under N$_2$ gas pressure. Under N$_2$ gas, the reaction solution was stirred for 1 h. With the aid of a magnet, the solution was collected and washed with ethanol to remove the excess NaBH$_4$ and iron salt. To obtain rGO/Fe^0, the nanocomposite was dried at 60 °C in a vacuum oven for 12 h. Under an atmosphere of N$_2$, the dried material was heated to 400 °C for 2 h to obtain rGO Fe^0/Fe$_3$O$_4$ [24].

2.2.3. Preparation of rGO/Fe^0/Fe$_3$O$_4$/TiO$_2$

To synthesize rGO/Fe^0/Fe$_3$O$_4$/TiO$_2$ nanocomposites, the straightforward sol-gel method was used [31]. In brief, we dispersed 0.5 g of rGO/Fe^0/Fe$_3$O$_4$ in 350 mL of ethanol. For 30 min, the above solutions were sonicated. After that, 65 mL of titanium (IV) butoxide was added. The solution was stirred for another 2 h. A 250-mL Teflon-coated stainless steel autoclave with nitrogen purging was used,
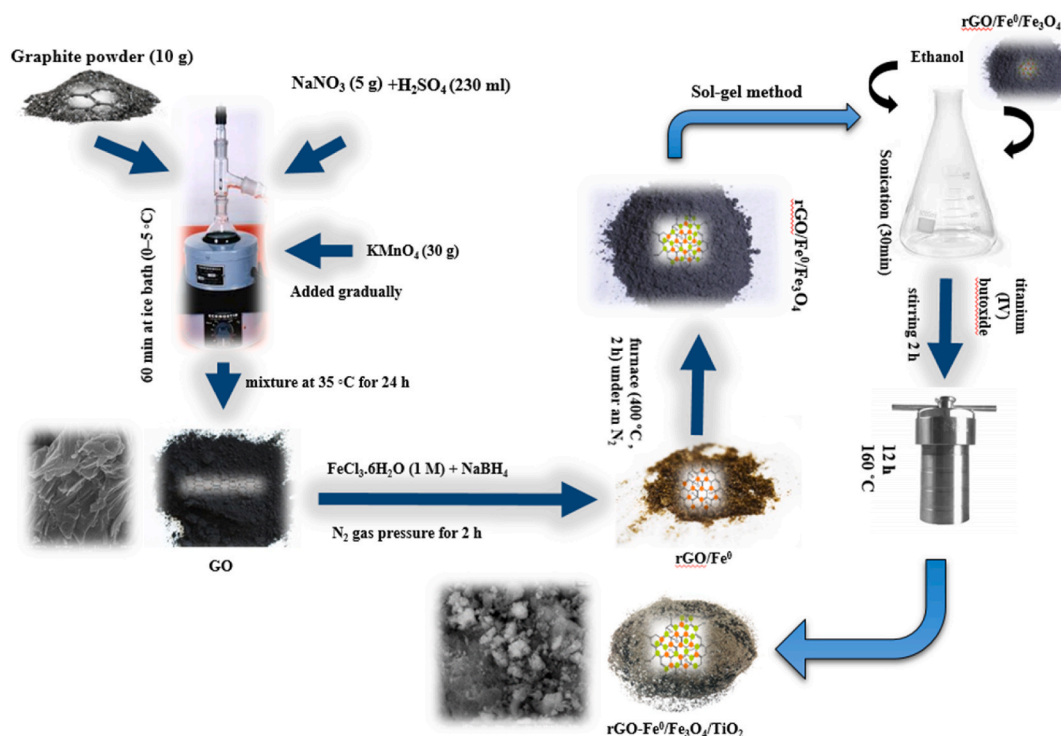
Fig. 1. Schematic of rGO, rGO/Fe^0, rGO/Fe^0/Fe$_3$O$_4$, and rGO/Fe^0/Fe$_3$O$_4$/TiO$_2$ synthesis.

in which the solution was heated for 12 h at 160 °C under nitrogen purging. Upon completion of the reaction, a precipitate of greyish color was acquired, and it was cleaned several times using ethanol and water. Afterward, the as-prepared nanocomposite was baked in a vacuum oven at 60 °C for 18 h. In (Fig. 1), the schematic of the catalyst synthesis steps is presented.

2.3. Characterization of rGO, rGO/Fe^0, rGO/Fe^0/Fe$_3$O$_4$, and rGO/Fe^0/Fe$_3$O$_4$/TiO$_2$

To assess of as-synthesized rGO, rGO/Fe^0, rGO/Fe^0/Fe$_3$O$_4$, and rGO/Fe^0/Fe$_3$O$_4$/TiO$_2$, FT-IR spectrophotometer (Spotlight 200i FT-IR Microscopy Systems; 4000-400 cm^{-1}) was utilized to explore the functional groups. X-ray diffraction (XRD) patterns were recorded on XRD diffractometer Rigaku- ZSX Primus 400; radiations source: Cu Kα [(λ = 1.54056 Å) monochromatic incident beam in the range of 10° to 80° with the step interval of 0.02°, and rate of 0.05°/s)] for the assess crystal structure of the structures. Also, the average crystallite size (D) of the prepared nanocomposite can be calculated from the Debye–Scherrer equation (Eq. 1) [32].

$$D = \frac{0.9\,\lambda}{\beta\,cos\,\theta} \tag{1}$$

A UV–vis spectrophotometer (DRS, Lambda 950, USA) was used to determine the diffuse reflectance absorption spectra of the rGO, rGO/Fe^0, rGO-Fe^0/Fe$_3$O$_4$, and rGO-Fe^0/Fe$_3$O$_4$/TiO$_2$. To calculate the band gap, we used the Tauc formula (Eq. 2) [33].

$$(\grave{\alpha}h\upsilon)^2 = A\left(h\upsilon - E_g\right) \tag{2}$$

The surface morphology of the samples was observed with a field-emission scanning electron microscope (FE-SEM) (UN41219SEM) under vacuum conditions ≥1.3 × 10^{-4} mbar. To analyze the purity and elemental composition of samples, energy dispersive spectroscopy (EDS) was applied. Additionally, the samples were analyzed using a transmission electron microscope (TEM) operating at 200 kV (TEM Model CM200, SUPERTWIN). Quantachrome Autosorb analyzer (BET) was used to measure the special surface areas, volumes, and distribution pore sizes of catalysts at 77 K. Before the degassing process, samples were dried in situ at 200 °C under vacuum for 12 h. Brunauer–Emmet–Teller (BET) methods were used for calculating surface areas over a p/p$_0$ range. Magnetization curves of the samples were measured using an HH-18 vibrating sample magnetometer (VSM, MPMS-3 model, USA).

2.4. rGO-Fe^0/Fe$_3$O$_4$/TiO$_2$ point of zero charge measurements

A total of 6 Erlenmeyer containing 25 mL of distilled water with pH values ranging from 2 to 12 were prepared to determine the potential of zero charges (pH$_{pzc}$) of rGO/Fe^0/Fe$_3$O$_4$/TiO$_2$ nanocomposite. To the solutions was added 0.25 g of the nanocomposite. A second pH reading was performed after 24 h had passed.

2.5. Experiments set-up

To evaluate the performance of the synthesized nanocomposite, PNG was selected as the target pollutant. All test steps were performed at ambient pressure and temperature (25 ± 2 °C). In this study, a horizontal rectangular cubic glass photocatalytic reactor with a useful volume of 500 mL was used. In the middle of the reactor, a quartz sheath contained the light source. The reactor was placed inside a polyvinyl chloride (PVC) box to control the emission of light. The stock solution (1000 mg/L) was prepared from PNG powder and different concentrations of antibiotics were prepared from the stock solution. The pH of the samples was adjusted by sulfuric acid and sodium hydroxide (0.1 N). A pH meter (HI-110 - Canada) was used to adjust the pH of the solutions. The nanocomposite was added at the end of sample preparation and the process was started. Homogeneous mixing inside the reactor was performed by a mechanical stirrer. At room temperature and atmospheric pressure, all experiments were conducted. The quartz-glass jacket needed to be equipped with a continuous flow of condensation to lower the lamp's temperature during irradiation. At the end of each step of the process, sampling was performed by pipette and catalyst separated via centrifuge (XM-100, ARA co.), then the concentration of PNG was determined by high-performance liquid chromatography (HPLC). Finally, PNG removal, chemical oxygen demand (COD), and total organic carbon (TOC) performance were calculated via (Eq. (3)).

$$Decomposition\ performance\ (\%) = \frac{(C0 - Ce)}{C0} \times 100 \tag{3}$$

The initial and residual concentrations (mg/L) of PNG are given by C$_0$ and C$_e$.

2.6. Influence parameters, and optimization by CCD

Several factors were considered in this study to assess the effectiveness of PCP in PNG removal, including initial solution pH, nanocomposite dose, reaction time (RT), and PNG concentration. CCD was applied as an approach in response surface methodology (RSM) to determine the effect of these main parameters [34] on PCP efficiency. The parameters and their levels are illustrated in Table 1. To investigate the influence of the experimental factors on the degradation of PNG, we designed 30 runs of experiments using the CCD design.

According to (Eq. (4)), a second-order polynomial model was developed empirically to describe the removal of PNG via PCP [35].:

$$Y = \beta_0 + \sum_{i=1}^{k} \beta_i x_i + \sum_{i=1}^{k} \beta_{ii} x_i^2 + \sum_{i=1}^{k-1} \sum_{j=i+1}^{k} \beta_{ij} x_i x_j + \varepsilon \tag{4}$$

There is a response variable Y (%) corresponding to the removal of PNG (%), an intercept b$_0$, and coefficients i, ii, and ij of the linear, quadratic, and interaction effects of each variable, respectively, xi and xj representing codes representing experimental levels. As part of the comparison between factors with different units, coded values were obtained using (Eq. (5)).

$$x_i = \frac{X_i - X_0}{\Delta x} \tag{5}$$

It has coded values of xi, a difference between high and median values of x, actual values of the variables, and median values of X_0. To assess the statistical significance of the fitted models and to determine the interaction between response and factors studied, analysis of variance (ANOVA), p-value and F-value were performed. A correlation coefficient, including R^2, R^2_{adj}, and $R^2_{predict}$ was also used to evaluate. After optimization of the process, the pseudo-first-order kinetic of reaction (Eq. (6)) was used to determine and evaluate the constant rate (k, min^{-1}) of kinetics reaction profiles at different PNG concentrations, and COD and TOC studies, synergistic effect (SF) (Eq. (7)), changes occurred in during of optimum condition on scanning wavelength in the range of 190–400 nm, recovery, and reusability of the nanocomposite, the effect of different light source (UV–C, UV-A, and visible light), determine of adsorption share, the effect of organic, and inorganic radical scavengers, and by-products, probably pathways, and intermediates were investigated.

$$In\left(\frac{Ct}{C0}\right) = -Kt \tag{6}$$

C$_t$, C$_0$, K, and t are PNG concentration at t, PNG concentration at the start of the reaction (mg/L), rate constant (min^{-1}), and reaction time (min).

$$SF = \frac{PCP \ performance}{Sum \ of \ single \ mechanism \ performancr} \tag{7}$$

2.7. Analytical methods

An HPLC system with a UV–vis detector (Shimadzu LC-20) and a C18 column (Zorbax SB-C18, Agilent Technologies) was used to determine PNG concentration. 0.4 mL/min flow rates were used for mobile phases A and B, respectively, consisting of acetonitrile and water with 0.1% formic acid. 20 mL of each sample after the process was injected. A 220 nm wavelength was used for the detection of PNG. For the PNG, the retention time is 5.8 min. The detection and quantification limits (LOD and LOQ) were calculated based on the standard deviation of the response and the slope of the calibration curves. Analytikjena's multi-C/N 3100 TOC analyzer was used to measure the concentrations of TOC. The COD was measured using a spectrophotometer (DR6000-HACH, USA (5220-C; closed-reflux) [36].

3. Results and discussion

3.1. Characterization of rGO, rGO/Fe^0, rGO/Fe^0/Fe$_3$O$_4$, and rGO/Fe^0/Fe$_3$O$_4$/TiO$_2$

3.1.1. FT-IR
Based on FT-IR analysis, the functional groups on the surface of samples were investigated between 4000 and 500 cm^{-1} (Fig. 2).

An application of FT-IR spectroscopy is to analyze materials qualitatively, in particular, to identify and detect functional groups in organic compounds. The results indicate that the rGO FT-IR spectra exhibit peaks at 3440 cm^{-1}, which correspond to the O–H tensile band, and peaks at 1724, 1626, and 1034 cm^{-1}, which correspond to the C═O, C═C, and C–O–C vibrations, respectively. The peak band intensities of the oxidized groups were reduced in rGO/Fe^0 FT-IR spectra. In this case, sodium borohydride may have reduced oxygen-containing groups. In the rGO/Fe^0/Fe$_3$O$_4$ spectrum, all bands related to rGO/Fe^0 were also observed, including the peak of Fe–O tensile vibration at 582 cm^{-1}. The FT-IR spectra of rGO/Fe^0/Fe$_3$O$_4$/TiO$_2$ show wide peaks in the range of 750-700, which are indicative of TiO$_2$ coating on rGO/Fe^0/Fe$_3$O$_4$. In previous studies, similar results have been reported. A study by Cakmak and co-workers reported that the GO surface contains several functional groups, such as hydroxyls, epoxides, and carboxyls. An overlap between the Fe–O and Ti–O vibrations at 500-700 cm^{-1} was observed on the titanium dioxide/magnetite nanocomposite [31].

Table 1
Parameters and their levels in PCP optimization.

Factors	Names	Units.	Min	Max	Coded low	Coded high	Mean	Std. Dev.
A	pH	–	2	10	$-1 \leftrightarrow 4$	$+1 \leftrightarrow 8$	6	1.82
B	Dose	mg/L	5	25	$-1 \leftrightarrow 10$	$+1 \leftrightarrow 20$	15	4.55
C	PNG Con	mg/L	25	125	$-1 \leftrightarrow 50$	$+1 \leftrightarrow 100$	75	22.74
D	Time	min	15	75	$-1 \leftrightarrow 30$	$+1 \leftrightarrow 60$	45	13.65
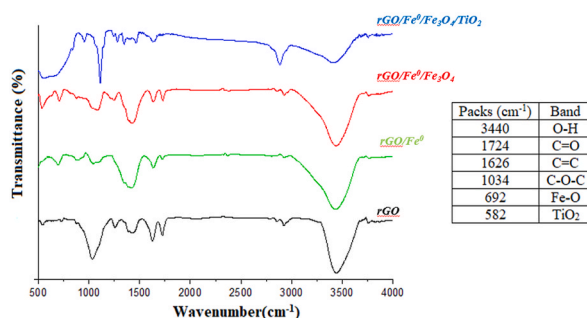
Fig. 2. FT-IR spectra of GO, rGO/Fe^0, rGO/Fe^0/Fe$_3$O$_4$, rGO/Fe^0/Fe$_3$O$_4$/TiO$_2$.

3.1.2. XRD

XRD analysis was applied to determine the crystalline properties of the samples (rGO, rGO/Fe^0, rGO/Fe^0/Fe$_3$O$_4$, and rGO/-Fe^0/Fe$_3$O$_4$/TiO$_2$) (Fig. 3).

An apparent sharp diffraction peak was observed at the value of 10.50 in the rGO XRD pattern. According to the (JCPDS 41–1487), based on the modified hummer's method, this peak could be assigned to the (001) plane of graphite oxide. As a result of the oxidation, the graphite structure was destroyed, confirming that graphite powder had been converted to the graphitic oxide by this peak [37]. During the oxidation of graphite powder, numerous functional groups are formed, which are bonded on the edges and both sides of the basal plane. The results of Pudukudy and coworkers' study confirm the results of this study [38]. An XRD analysis confirmed the successful incorporation of Fe^0/Fe$_3$O$_4$/TiO$_2$ onto GO sheets. The diffraction peaks at 25.68, 37.62, 53.96, 62.46, 68.48, 71.01, and 75.12 were indexed to the (101), (004), (105), (213), (116), and (220) planes of anatase TiO$_2$ (JCPDS 21–1272), respectively [39]. The result of this study was similar to Nguyen and coworkers' study [40]. Also, reflections were observed at 2θ = 31.5, 35.9, 54.3, 56.78, and 62.8 corresponding to the respective (220), (311), (422), (511), and (440) planes of cubic Fe$_3$O$_4$ and (JCPDS NO.19-0629), and reflections at 45.69(100) and 64.31(200) associated with Fe^0(JCPDS NO.87-0721) [24].

3.1.3. FESEM, EDX, and TEM

The morphologies information of GO and rGO/Fe^0/Fe$_3$O$_4$/TiO$_2$ were illustrated in (Fig. 4).

The FESEM image of rGO (A-1, and A-2) has revealed a flaky surface, an ordered layer of pristine graphite is oxidized, resulting in this condition. More details of the morphology of rGO can be presented by TEM image (A-3). The TEM image confirms the rGO sheet in structure. The Energy-dispersive X-ray spectroscopy (EDX) image (A-4), showed that carbon and oxygen were the main elements in rGO. The obtained results were similar to Baghchesara and coworkers' study [41]. At rGO/Fe^0/Fe$_3$O$_4$/TiO$_2$ FESEM images (B-1, and B-2), and TEM image (B-3), it was found that well-distributed crystalline TiO$_2$ was formed on rGO sheets and a core-shell nanocomposite was fabricated. Also, EDX result (B-4), showed that carbon (6.62 W%), oxygen (32.45 W%), titanium (43.47 W%), and iron (17.46 W%) were major elements in rGO/Fe^0/Fe$_3$O$_4$/TiO$_2$. Boruah et al. also found similar results [42].

3.1.4. VSM, BET, and UV–vis spectra

At room temperature, rGO/Fe^0/Fe$_3$O$_4$ and rGO/Fe^0/Fe$_3$O$_4$/TiO$_2$ were analyzed for their magnetic properties (Fig. 5a). rGO/Fe^0/Fe$_3$O$_4$/TiO$_2$ had saturation magnetizations of approximately 40.5 and 15.5 emu. g^{-1}, respectively. The phenomenon is primarily due to the presence of the rGO wrapped around Fe$_3$O$_4$ and the subsequent anchoring of TiO$_2$ nanoparticles on the surface. While rGO/Fe^0/Fe$_3$O$_4$/TiO$_2$ had a lower saturation magnetization value than rGO/Fe^0/Fe$_3$O$_4$, it was strong enough to collect from aqueous solutions. In previous studies, the magnetic properties of nanocomposite materials formed with TiO$_2$ and other particles have been reported to be reduced when coated with magnetic or paramagnetic particles. Fan and coworkers' study found that the magnetic saturation values of
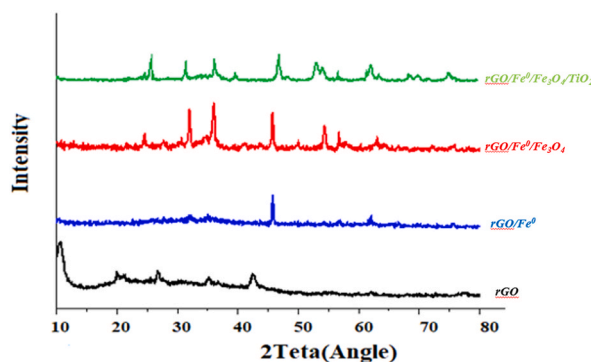
Fig. 3. XRD pattern of GO, rGO/Fe^0, rGO/Fe^0/Fe$_3$O$_4$, rGO/Fe^0/Fe$_3$O$_4$/TiO$_2$.
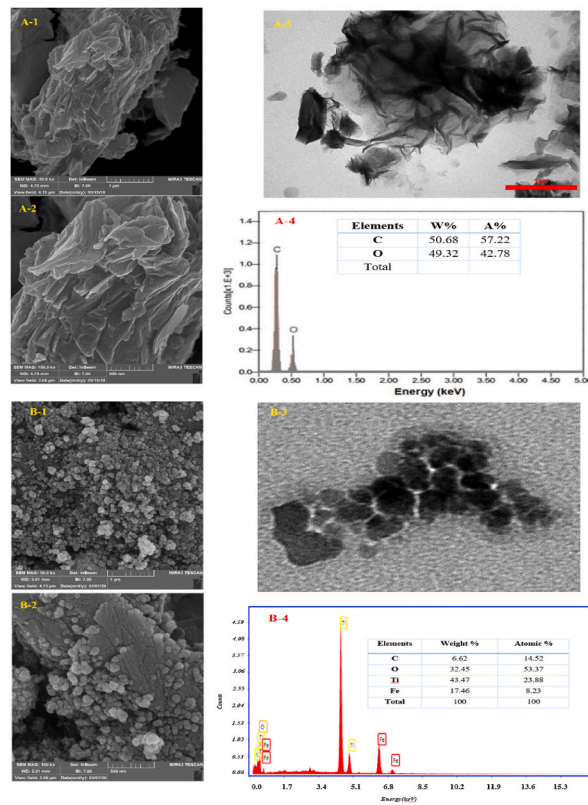
Fig. 4. FESEM, TEM, and EDX of rGO and rGO/Fe^0/Fe$_3$O$_4$/TiO$_2$.

pure Fe$_3$O$_4$, Fe$_3$O$_4$TiO$_2$/RGO-1, 2, and 3 nanocomposites were 50.09, 11.37, 39.2, and 42.11, respectively [43]. A spectrum of diffuse reflectance (220–720 nm) for pure TiO$_2$, rGO, and rGO/Fe^0/Fe$_3$O$_4$/TiO$_2$ is shown in (Fig. 5b). There was significant absorption in the UV-C region for pure TiO$_2$, rGO, and rGO/Fe^0/Fe$_3$O$_4$/TiO$_2$, but at UV-A, TiO$_2$, and rGO-Fe^0/Fe$_3$O$_4$/TiO$_2$ were remarkably absorbed, while at the visible range, only rGO/Fe^0/Fe$_3$O$_4$/TiO$_2$ was remarkably absorbed. According to the Tauc formula, the bandgap for pure TiO$_2$ and rGO/Fe^0/Fe$_3$O$_4$/TiO$_2$ is 3.2 eV, whereas that for rGO/Fe^0/Fe$_3$O$_4$/TiO$_2$ is 2.2 eV. Compared to pure TiO$_2$, rGO/Fe^0/-Fe$_3$O$_4$/TiO$_2$ composite has a significantly lower band gap energy. In the rGO/Fe^0/Fe$_3$O$_4$/TiO$_2$ composite, the band gap narrowed to a greater extent due to the formation of the Ti–O–C bond and core-shell structure, which created a new molecular orbital. Under UV-A
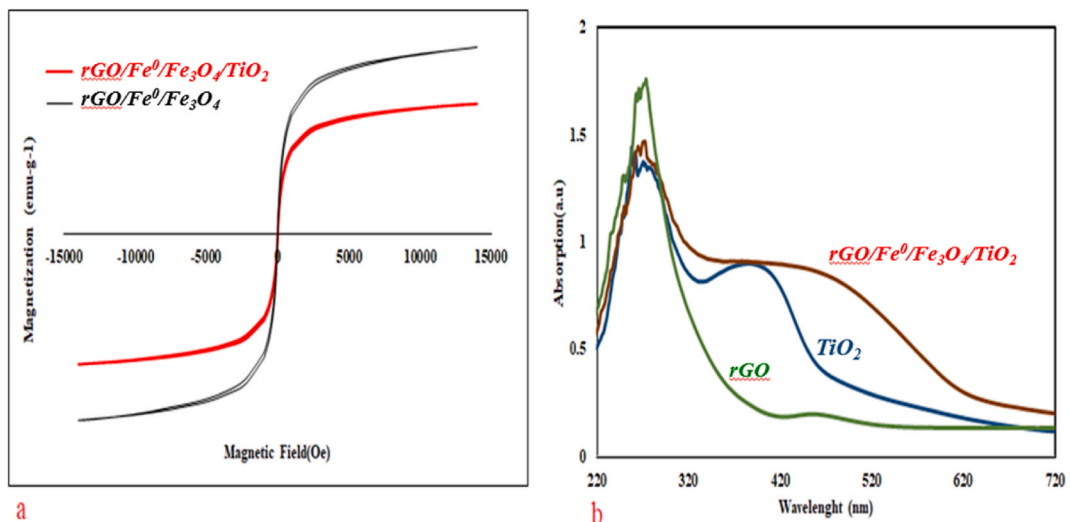
Fig. 5. a) VSM of rGO/Fe^0/Fe$_3$O$_4$, and rGO/Fe^0/Fe$_3$O$_4$/TiO$_2$. b) UV–vis diffuse reflectance spectra of rGO, pure TiO$_2$, and rGO/Fe^0/Fe$_3$O$_4$/TiO$_2$.

and visible light irradiation, the band gap between the rGO/Fe^0/Fe$_3$O$_4$/TiO$_2$ composite may narrow, resulting in better photocatalytic activity. The bandgaps of TiO$_2$, TiO$_2$–Fe$_3$O$_4$/graphene, and TiO$_2$–TiO$_2$–Fe$_3$O$_4$/graphene were reported by Li and coworkers to be 3.12 eV and 2.12 eV, respectively [44].

The specific surface area of the composite rGO/Fe^0/Fe$_3$O$_4$/TiO$_2$ was calculated based on N$_2$ adsorption-desorption measurements and BET analysis (Fig. 6). rGO/Fe^0/Fe$_3$O$_4$/TiO$_2$ reveals a type IV N$_2$ adsorption-desorption isotherm with H$_3$ hysteresis loop. Table 2 lists the parameters of pore structure. rGO/Fe^0/Fe$_3$O$_4$/TiO$_2$ composite has a maximum specific surface area of 74.42 m^2 g^{-1}. There have been different results reported in the last literature. In Fan and coworkers' study area of Fe$_3$O$_4$–TiO$_2$/RGO nanomaterial, 183.33 m^2 g^{-1} was reported [43].

3.2. Development of the design, the fitting process, and the statistical analysis of the CCD

To determine the condition conducive to optimal performance of the decomposition of PNG by PCP, a statistical analysis of the responses presented in Table 3 was performed. The variables of pH, nanocomposite dose, initial PNG concentration, and reaction time were considered the main variables, and the UA lamp with an intensity of 16 ($\lambda = 385$ nm) was considered constant in all runs. According to the results, PCP is effective in removing PNG in a range of 57.6 to 95.3% (mean 77.37%). Fisher variance ratios and F-values are substantiated statistical indexes used in the ANOVA analysis to adjust how to fit factors representing deviations. A statistically significant model based on these indices, namely an F-value (>0.9) and a P-value (0.05), was selected. Design experts presented a quadratic model based on tests that describe the relationship between predicted and experimental values (Table 4).

According to Table 5, the ANOVA results for the quadratic regression model indicate a high reliability and a low probability value, suggesting that the coded relationship between actual data and predicted values can be justified. The correlation coefficient values (i. e., R2, R2adj, and R2predict) were much higher than those achieved for other models, confirming the model's extraordinary validity and efficiency. With an R2 of 0.98, the quadratic model can explain more than 98% of the total variability, and less than 2% of the data are descriptive. There is a perfect correlation between R2, R2adj, and R2predict, indicating that the model is capable of predicting responses accurately [45,46].

As described below, the polynomial equation corresponding to PNG removal (%) is represented as coded factors (Eq. (8)):

$$
\begin{aligned}
\text{PNG removal}(\%) = {} & 63.12 + (4.5 \times \text{pH}) + (0.4 \times \text{Dose}) - (0.3 \times \text{PNG}) + (0.07 \times \text{Time}) - (0.15 \times \text{pH} \times \text{Dose}) - (0.02 \times \text{pH} \times \text{PNG}) \\
& + (0.011 \times \text{Dose} \times \text{PNG}) + (0.006 \times \text{PNG} \times \text{Time}) - (0.1875 \times \text{pH}^2) + (0.015 \times \text{Dose}^2) + (0.0006 \times \text{PNG}^2) \\
& - (0.004 \times \text{Time}^2)
\end{aligned}
$$

$$(8)$$

As shown in (Fig. 8), the studied mediators had both positive and negative effects on the removal of PNG. Even though the co-efficient of variation (CV) was low for the quadratic model, this confirms the precision of the experiments and the reproducibility of the model [48].

3.3. The impact of parameters on the PNG removal at PCP

Fig. 7, illustrated the effect of pH, nanocomposite dose (Fig. 7a), initial concentration of PNG (Fig. 7b), and reaction time, values influence the PCP performance.
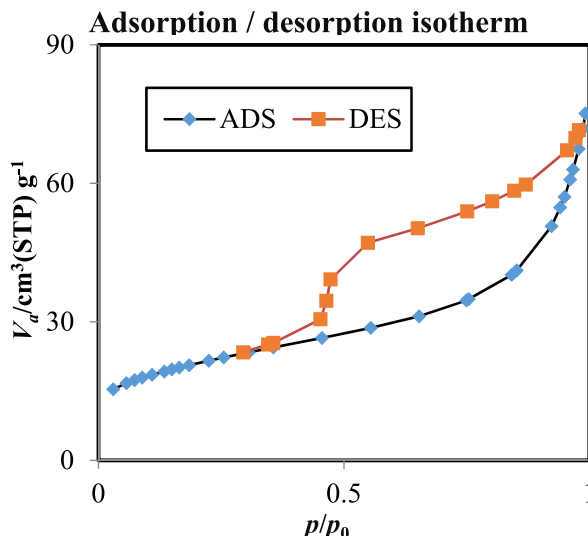
Fig. 6. Adsorption/desorption isotherm of rGO/Fe^0/Fe$_3$O$_4$/TiO$_2$.

Table 2
Summary of BET, Langmuir, t, and BJH test.

BET plot		
V_m	17.099	[cm^3(STP) g^{-1}]
$a_{s,BET}$	74.422	[m^2.g^{-1}]
C	223.23	
Total pore volume($p/p_0 = 0.990$)	0.1142	[cm^3.g^{-1}]
Mean pore diameter	6.1384	[nm]
Langmuir plot		
Vm	21.308	[cm^3(STP) g^{-1}]
$a_{s,Lang}$	92.741	[m^2.g^{-1}]
B	0.7995	
t plot		
Plot data	Adsorption branch	
a_1	79.11	[m^2.g^{-1}]
V_1	0	[cm^3.g^{-1}]
a_2	22.178	[m^2.g^{-1}]
V_2	0.045765	[cm^3.g^{-1}]
2t	1.5979	[nm]
BJH plot		
Plot data	Adsorption branch	
V_p	0.1031	[cm^3.g^{-1}]
$r_{p,peak}(Area)$	1.29	[nm]
a_p	47.29	[m^2.g^{-1}]

Table 3
Experiments designed by the CCD method and its results in the PCP.

Factors	Factor 1	Factor 2	Factor 3	Factor 4	Experimental performance
	A: pH	B: Dose	C: PNG con	D: Reaction time	
Unit	–	mg/L	mg/L	min	%
1	8	10	50	30	62
2	6	25	75	45	82.3
3	4	20	50	30	78
4	6	15	75	45	83
5	10	15	75	45	59.1
6	6	15	75	45	83
7	4	20	100	60	78.8
8	4	10	50	30	61.4
9	6	5	75	45	57.6
10	8	10	100	60	62.3
11	4	10	100	30	92.5
12	4	20	50	60	93.2
13	4	10	100	60	61.3
14	6	15	75	45	83
15	6	15	75	45	83.1
16	6	15	125	45	93.4
17	6	15	75	45	83.1
18	4	20	100	30	93.5
19	2	15	75	45	66.7
20	4	10	50	60	66
21	8	10	100	30	77.6
22	6	15	75	15	77.7
23	6	15	75	75	77.4
24	8	20	50	60	95.3
25	8	10	50	60	78.6
26	6	15	25	45	93
27	8	20	100	60	70.1
28	8	20	100	30	75.1
29	6	15	75	45	83
30	8	20	50	30	70.1

As can be observed, all parameters' influence on the removal performance is significant, and the highest removal performance of PNG (more than 90%) occurred. By increasing the pH of the solution to near 6.0, the degradation degree was increased considerably, but then clearly declined when the pH value was increased to 10.0 (Fig. 7a). As described in the literature, pH at PCP affects the absorption capacity and decomposition of organic compounds, the distribution of electricity on the catalyst's surface, and the valence band oxidation potential. Photocatalytic oxidation is dependent on ph. The catalyst's surface has various charges when pH is below or above zero. It was determined that pH$_{zpc}$ is approximately 6.5 in this study. As pH$_{zpc}$ increases and decreases, the catalyst surface has a

Table 4

Fit summary of the model.

Source	Sequential p-value	Lack of Fit p-value	Adjusted R^2	Predicted R^2	
Linear	0.1211	<0.0001	0.1242	−0.1550	
2FI	0.0085	<0.0001	0.4963	0.4643	
Quadratic	**< 0.0001**	**< 0.0001**	**0.9931**	**0.9794**	**Suggested**
Cubic	0.0038	<0.0001	0.9988	0.9571	Aliased

Table 5

ANOVA for the quadratic model of PCP in PNG removal.

Source	Sum of squares	df	Mean square	F-value	p-value	
Model	823.78	14	58.84	162.95	<0.0001	significant
A-pH	160.17	1	160.17	443.54	<0.0001	
B-Dose	240.67	1	240.67	666.46	<0.0001	
C-PNG Con	73.50	1	73.50	203.54	<0.0001	
D-Time	121.50	1	121.50	336.46	<0.0001	
AB	36.00	1	36.00	99.69	<0.0001	
AC	20.25	1	20.25	56.08	<0.0001	
BC	30.25	1	30.25	83.77	<0.0001	
CD	90.25	1	90.25	249.92	<0.0001	
A^2	15.43	1	15.43	42.73	<0.0001	
B^2	3.86	1	3.86	10.68	0.0052	
C^2	3.86	1	3.86	10.68	0.0052	
D^2	27.43	1	27.43	75.96	<0.0001	
Residual	5.42	15	0.3611			
Lack of Fit	5.42	10	0.5417	3.2	0.981	Not significant
Pure Error	0.0000	5	0.0000			
Cor Total	829.20	29				

Accordingly, the F-value is 162.95 and the *P*-value is 0.0001, which indicates the model is well suited to explain the amplification of the relationship between response values. In addition, the model discernment is satisfactory if the precision ratio is greater than 4.0 [47].
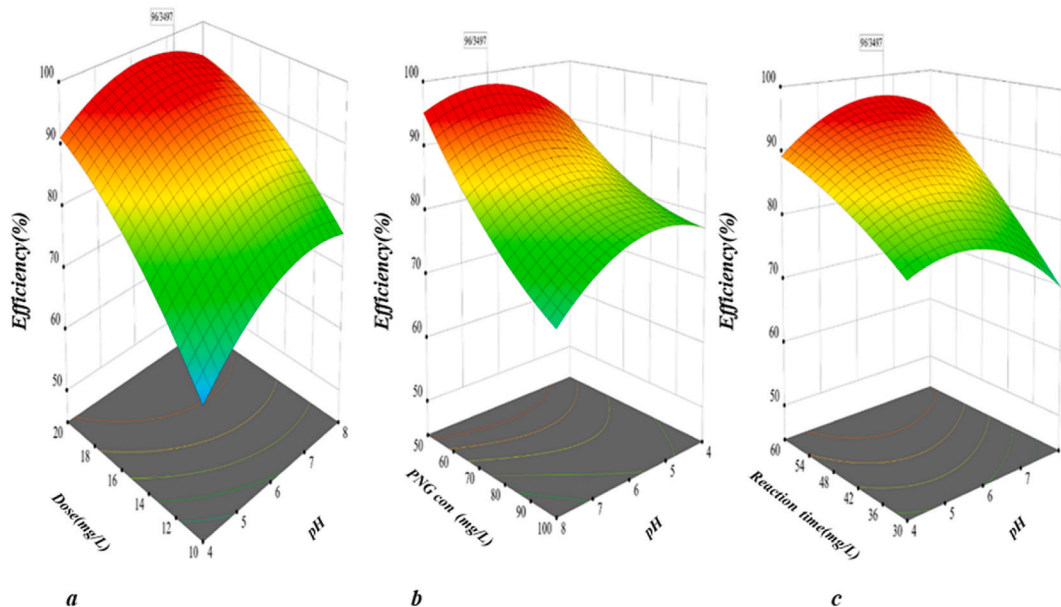
Fig. 7. Effect of parameters into PNG removal in PCP.

negative and positive charge. Catalyst surfaces are often colonized by H^+ ions at pH levels below 6.5. At pH levels above 6.5, the catalyst's surface is colonized by the OH^- ion. In the same way, a different charge is illustrated when pH is lower or higher than the pka of the material (pka PNG = 2.74). Therefore, both the catalyst and pollutants have different ionization states at different pH levels. Due to the nature of the catalyst employed, and PNG, the decomposition performance of PNG favored a near-neutral solution. It is important to note that the change in pH affects the isoelectric point or the surface load of the photocatalyst. PNG tends to become an
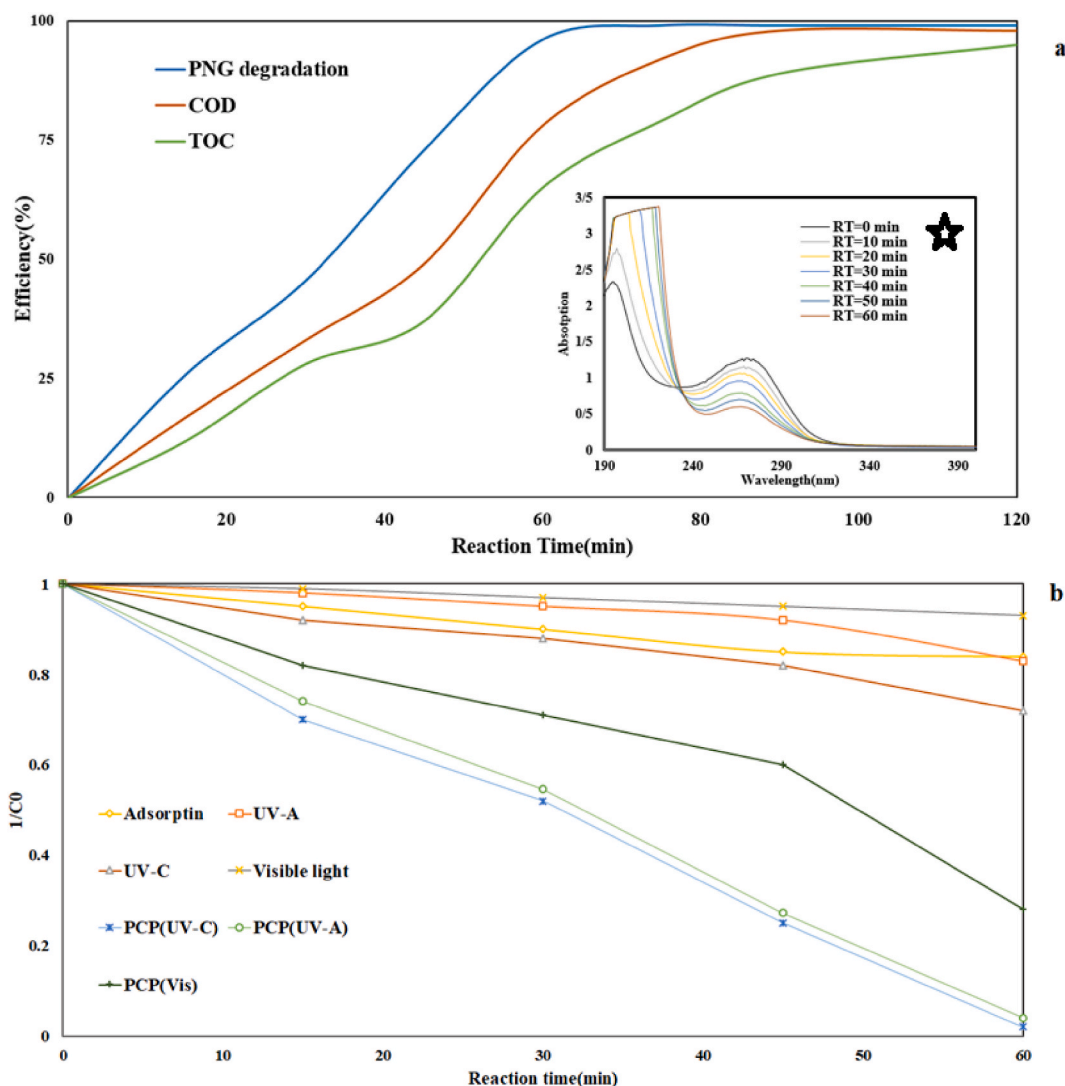
Fig. 8. a) COD and TOC removal efficiency, b) The synergistic effect of different mechanisms in PCP (pH = 6.5, RT = 59.1 min, PNG concentration = 52 mg/L, and catalyst dose = 18.5 mg/L).

anion if pH exceeds pka [49]. The electrostatic repulsion force between the catalyst and the PNG is generated if pH is greater than 6.5, given the negative surface charge of the catalyst and the anionic nature of PNG. Accordingly, the degradation of PNG is reduced. Nevertheless, other studies have demonstrated that pH directly influences radical production. In strongly acidic conditions, PNG degradation is decreased due to hydroxyl radical scavenging (Eq. (9)) [1].

$$H^+ + °OH + e^- \rightarrow H_2O \qquad (9)$$

Moreover, due to a reduction in the hydroxyl radical oxidation potential, and the formation of insoluble compounds, PNG degradation at alkaline pH is decreased. Therefore, increasing pH will result in hydrogen peroxide decaying and reducing ultraviolet radiation and radical hydroxyl production. Berkani and coworkers also reported that Penicillin G was best degraded by photocatalysis at a pH of 6.8 in an aqueous solution [7]. One of the other parameters investigated was the nanocomposite dose. A catalyst's dose affects the active site and the absorption of light [50]. As can be seen in (Fig. 7a), the PNG removal efficiency was improved by increasing the nanocomposite dose to 18.5 mg/L and then enforcing it. Increasing catalyst dosage increases the area of active sites, but increasing solution turbidity can reduce light penetration into the solution due to increasing catalyst dosage. As a result, the rate of PNG removal decreased. An optimum dose of ZNS of 0.5 g/L was reported in a study by Pouretedal et al. [51]. Pollution concentrations play an important role in the operation of processes. A study of the effect of initial concentrations of pollutants on the efficiency of a process is necessary due to the presence of different concentrations of pollutants, such as pharmaceutical compounds in the environment. PNG concentrations between 50 and 100 mg/L were investigated in this study. According to the results, the efficiency of the PCP decreased with increasing the initial concentration of PNG in the reaction medium (Fig. 7b). This is because as PNG molecules are

concentrated in the environment, the likelihood of exposure to direct or indirect oxidizing agents decreases. There is a decrease in the probability of degradation of PNG as the number of PNG molecules oxidizing free radicals increases. During PCP, the presence of intermediate and organic compounds increases as there is a decreasing chance of complete oxidation. Similarly, Kamranifar and coworkers examined the photocatalytic capabilities of penicillin G at various concentrations (10–100 mg/L) in their study. At 10 mg/L, the highest performance was achieved (70.7%) [1]. PCP is also influenced by reaction time. This study examined the degradation of PNG over 30–60 min. In the study, it was found that the removal efficiency of PNG increases with an increase in reaction time (Fig. 7c). By increasing the reaction time, more hydroxyl radicals and electron-hole pairs are formed in the PCP, increasing the rate of PNG degradation by direct and indirect oxidation, and therefore increasing the efficiency of the process. The effect of reaction time has been investigated in previous studies. According to Al-Musawi, 60 min is the optimum reaction time for Ampicillin degradation [52]. Finally, after the optimization of PCP via CCD, optimal condition was determined as pH~ 6.5, catalyst dose 18.5 mg/L, reaction time 59.1 min, and initial PNG concentration 52 mg/L. In these condition, the PCP was able to achieve 96% of the initial PNG concentration degradation.

3.4. Additional studies in optimal conditions

3.4.1. COD, TOC removal, changing in wavelength scan, determine the catalyst components efficiency on PNG degradation, and synergistic effect

COD and TOC tests are relatively suitable indicators for determining the mineralization of organic pollutants in advanced oxidation processes. In this study, these two indicators were investigated. Under optimal conditions, the photocatalytic process can remove 78% of the COD and 65% of the TOC from the PNG (Fig. 8a). Since degradation of PNG into intermediates may occur in the PCP, it is obvious that the rate of reduction of COD and TOC indicators was always less than the removal of PNG. To more efficient removal of COD and TOC, a higher reaction time was required. Within 120 min reaction time, more than 99% of PNG, more than 90% of COD, and TOC were decreased. In Aanchal Rathi and coworkers' study, metronidazole, COD, and TOC declined 72, 68, and 62%, respectively [53]. Absorption changes in wavelength scanning during the reaction time are presented in (Fig. 8 a*). According to the results, the rate of absorption varied at 0–60 min in the PCP process. Pirzada and coworkers study the Rhodamine B and p-Chlorophenol photo-degradation under solar light in the presence of LaFeO$_3$/Ag$_2$CO$_3$ nanocomposites. The results show that in the period from 0 to 45 min, noticeable changes in absorption spectra have occurred and the concentration of pollutants has decreased [54].

Herein, the role of all applied mechanisms in PCP in the PNG degradation in the two systems was conducted separately and concurrently under optimal conditions, and the related results are illustrated in (Fig. 8b). Adsorption and photolysis (UV–C, UV-A, and visible light) were influence mechanisms in PCP. As you can see, all of mechanisms had very lower efficiency in PNG degradation separately. Sorption, UV-A, UV-C, visible light photolysis, PCP(UV-C), PCP (UV- A), and PCP(vis-light) were 10, 12, 25, 7, 98, 96, and 72% efficiency respectively. The SF coefficient to PCP(UV-A), PCP(UV-C), and PCP(Vis) were investigated 4.36, 2.57, and 4.23 respectively. The results of determining the synergistic effect showed with the simultaneous presence of light source and catalyst in the PCP, the main mechanism of PNG degradation was indirect oxidation by free radicals and electron-hole pairs. The reason for the higher efficiency of the process in the presence of UV-C was the further oxidation by photolysis. In Yu and coworkers' study, SF in
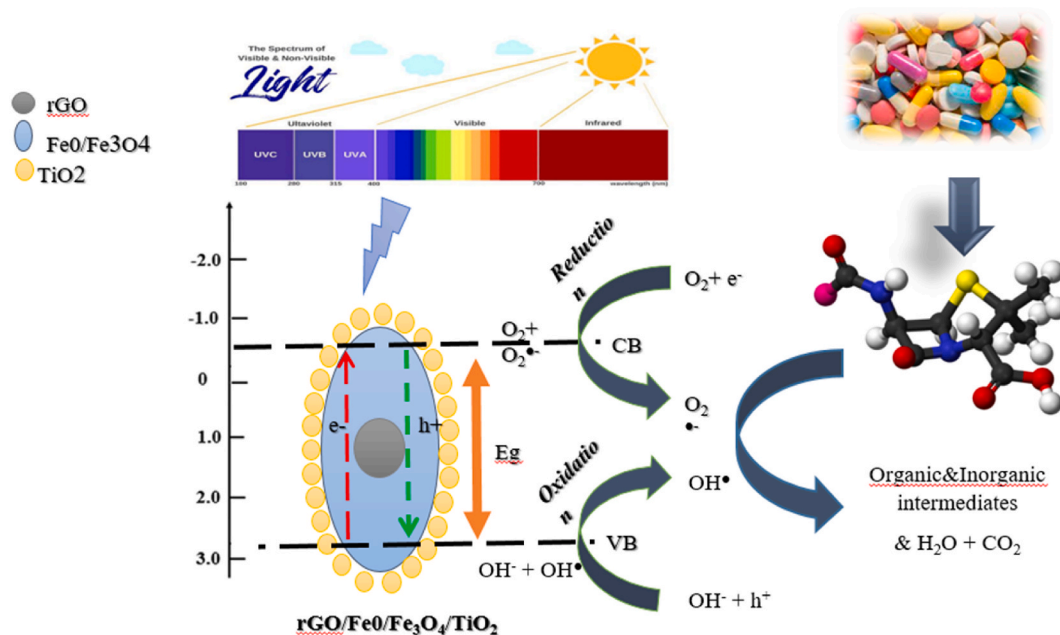
Fig. 9. Mechanism of PNG degradation by PCP- rGO/Fe^0/Fe$_3$O$_4$/TiO$_2$ system.

photocatalyst process for Oxytetracycline (OTC) removal 4.64 reported. The electrons accumulated on the catalyst, and generating reactive oxidant species (ROS_s) were reasons for the synergistic degradation of OTC by this process [55].

3.4.2. Photocatalytic degradation mechanism of PNG, radical scavengers effect on PCP, recovery, and reusability of catalyst

An explanation for the degradation of PNG by PCP-rGO/Fe^0/Fe_3O_4/TiO_2 systems has been proposed, and a schematic is shown in (Fig. 9). Different components in the synthesized nanocomposite have unique properties and specific activities. Graphene, a unique sp^2 hybrid carbon network material, including graphene oxide (GO) and reduced graphene oxide (rGO), has been used as an ideal cocatalyst or support for improving photocatalytic efficiency due to its high electron mobility, large surface area, and high transparency. Photo-induced electrons are quickly transferred from the conduction band of TiO_2 to its surfaces in rGO/TiO_2 due to the excellent electron acceptor properties of rGO sheets [56]. As Fe^0 in the composite can trap electrons generated from TiO_2 photocatalysis via Fe^{3+}/Fe^{2+} and Fe^{2+}/Fe^0 half-reactions, it prevents electron-hole recombination. Fe^0 with TiO_2 was expected to preserve Fe^0's reduction reactivity and improve its stability and mobility by preventing the formation of oxide layers on its surface [28]. The separation of TiO_2 from aqueous solutions has been reported as an important drawback in studies. To facilitate photocatalytic recollection in magnetic fields, doping of magnetic materials has been proposed. For this purpose, ferriferous oxide (Fe_3O_4) can be doped on semiconductors [57]. Furthermore, the first step is to adhere PNG molecules to the surface of the rGO/Fe^0/Fe_3O_4/TiO_2 photocatalyst in the reaction medium (Eq. (10)). Meanwhile, a hole (h^+) has been created within the valence band (VB) of rGO/-Fe^0/Fe_3O_4/TiO_2 nanocomposite as a result of the absorption of energy photons. (Eq. (11)). From the oxygen presence in aqueous, electrons were immediately transferred to reduce e^-/h^+ recombination (Eq. (12)). As a result of the holes (h^+) in the VB band, H_2O molecules decompose into oxygen and water (Eq. (13)). All ROSs produced, including $°OH$, h^+, and $O_2^{•-}$, attack the aliphatic and aromatic rings of PNG on the nanocomposite reaction site. PNG molecules are oxidized by all radicals to intermediates, CO_2, and H_2O (Eq. (14)) [58]. It is believed that the enhanced photocatalytic activity results from a synergistic interaction between nanostructured TiO_2 and Fe_3O_4 with rGO and their catalytic activity. In this case, PNG degradation can occur through several different methods, including the direct attack by the hydroxyl radical, direct reduction by photo-induced electrons, or direct oxidation in presence of holes. Due to strong van der Waal interactions, rGO sheets tend to agglomerate back into the graphitic structure. In this case, TiO_2 is incorporated on the surface of the graphene sheet to reduce agglomeration. Additionally, the interlink between TiO_2 and rGO during photocatalysis allows easy electron transfer, which improves the separation of charge carriers and hence the activity of the catalyst. Eventually, Fe_3O_4 increases degradation rate by adsorbing pollutants onto nanocomposite surfaces. The magnetic properties of Fe_3O_4 also make it useful for magnetic separation of nanocomposite photocatalysts from dispersions. As a result, the incorporation of TiO_2, Fe^0, and Fe_3O_4 into rGO enhances its photocatalytic activity. Similar results were reported in Benjwal and coworkers' study. In this study use of rGO/Fe_3O_4/TiO_2 nanocomposite to Methylene Blue degradation. Based on the results, the ternary nanocomposite (rGO–Fe_3O_4–TiO_2) exhibits the highest dye degradation efficiency (100% within 5 min) when compared to single and binary nanocomposite. A synergetic interaction between rGO and Fe_3O_4 and TiO_2 is responsible for this enhancement [37]. In Banerjee and coworkers' study, similar results were reported [59].

$$rGO / Fe^0 / Fe_3O_4 / TiO_2 + PNG \rightarrow PNG - rGO / Fe^0 / Fe_3O_4 / TiO_2 \tag{10}$$

$$rGO / Fe^0 / Fe_3O_4 / TiO_2 + h\upsilon \rightarrow rGO / Fe^0 / Fe_3O_4 / TiO_2 \left(e_{CB}^- + h_{VB}^+\right) \tag{11}$$

$$rGO / Fe^0 / Fe_3O_4 / TiO_2 \left(e_{CB}^-\right) + O_2 \rightarrow O_2^{•-} + rGO / Fe^0 / Fe_3O_4 / TiO_2 \tag{12}$$

$$rGO / Fe^0 / Fe_3O_4 / TiO_2 \left(h_{VB}^+\right) + H_2O \rightarrow °OH + H^+ \tag{13}$$

$$O_2^{•-} + °OH + h^+ + PNG \rightarrow \text{organic and inorganic intermediates} + CO_2 + H_2O \tag{14}$$
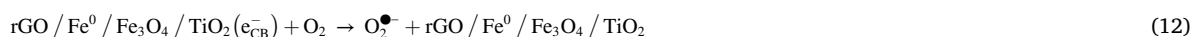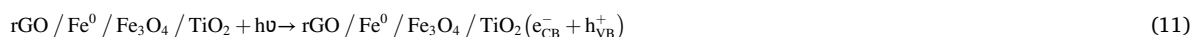
To investigate the main active radicals produced by the nanocomposite during PCP for the degradation of PNG, radical trapping experiments were conducted (Fig. 10a). A quencher for superoxide radicals is p-benzoquinone (BQ), whereas ethylenediaminetetra-acetate acid disodium (EDTA-2Na) and tertbutanol (t-BuOH) are applied as quenchers for the hole radical and the hydroxyl radical ($°OH$). The degradation efficiency of PNG was negligibly affected by EDTA-2Na, Accordingly, h^+ plays a virtually insignificant role in the reaction system. A reduction in the degradation rate of PNG was observed following the addition of t-BuOH, indicating that $°OH$ plays a critical role in the catalytic reaction. Nevertheless, the PCP performance was extremely shown with the addition of BQ, suggesting that $O_2^{•-}$ has a powerful role in PNG decomposition. PNG was more immediately removed with the $O_2^{•-}$ and $°OH$ radicals in the PCP. A similar result was reported in a study by Saravanakumar and co-workers [60]. For the application of photocatalysts, stability, reusability, and recyclability are vital parameters. According to (Fig. 10 b), the degradation activity of the rGO/Fe^0/-Fe_3O_4/TiO_2 nanocomposite did not significantly decrease at the fifth cycle under visible light irradiation, indicating that the nanocomposite exhibits suitable photocatalytic stability. In Albornoz and coworkers' study, the stability of SnO_2-doped TiO_2 catalyst was investigated. Based on the results of this study, the catalyst had 44 h stability in the photocatalyst process [61].

3.4.3. Study of the kinetics of reaction

An empirical model of PNG degradation in PCP is constructed to describe the experimental data (Eq. (6)) was developed under optimized conditions and at different concentrations of antibiotic. A linear pseudo-first-order kinetic model for PNG degradation over PCP is shown in (Fig. 11) and Table 6. At 100 mg/L concentration, there was a significant correlation between the experimental data
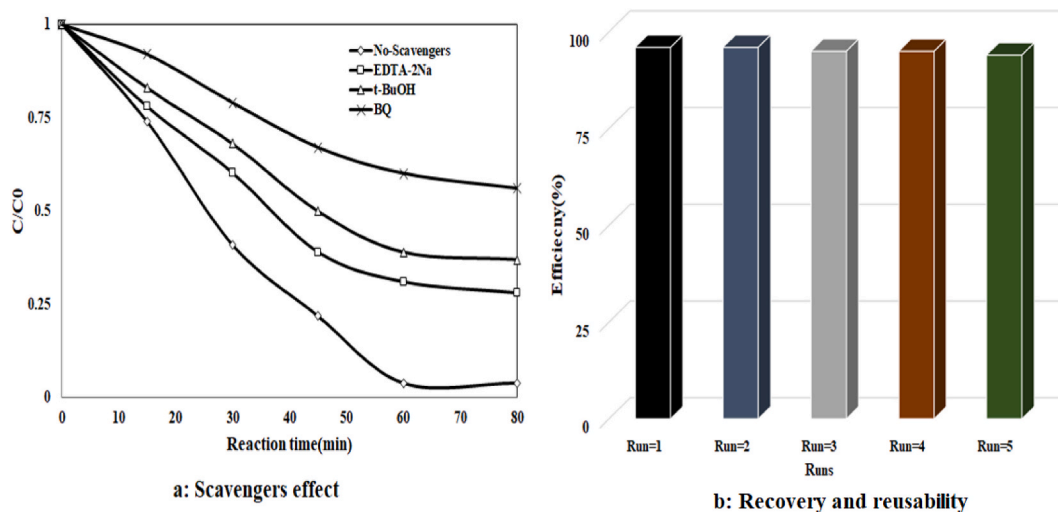
Fig. 10. a) Scavengers effect on PCP performance, b) Recovery and reusability of nanocomposite in PCP (pH = 6.5, RT = 59.1 min, PNG concentration = 52 mg/L, and catalyst dose = 18.5 mg/L).

and the pseudo-first-order kinetic ($R^2 > 0.98$). It was found that the apparent rate constant of PNG decomposition was 1.8 min^{-1} under these conditions. In Sekaran and coworkers' study, the degradation of acid blue 113 dye via photocatalysis process followed pseudo-first-order kinetic ($R^2 > 0.99$) [62].

3.4.4. Mineralization of PNG and by-products studies

To investigate the intermediate and by-products and probably reaction pathways of PNG degradation at optimal conditions, the GC-MS was used according to the instructions provided in the materials and methods section. According to the results of GC-MS analysis and (Fig. 12), the PNG and several by-products were detected.

As a result of the oxidation of PNG, seven important intermediate products were Phenoxyacetaldehyde, Acetanilide, Diacetamate, Phenylalanylglycine, N-Acetyl-L-phenylalanine, Diformyldapsone, and Succisulfone. PNG degradation over a photocatalytic process has previously identified those by-products as intermediate compounds [7]. It was conceivable to attempt the transmutation pathways of PNG over the PCP process as an AOPs based on Free radicals, and electron-hole pairs (Fig. 13). This figure illustrates two possible pathways for PNG photodegradation in PCP. PNG consists of a five-membered thiazolidine ring fused to a strained lactam ring. There is substantial research indicating that this antibiotic ring is chemically unstable and susceptible to extreme conditions, including heat, acids, bases, UV light, nucleophiles, and enzymatic reactions in which the hydrolytic ring opens, resulting in a loss of antibiotic activity. The similar result was reported in Berkani and coworkers' study [7]. Based on the review of previous studies, it was found that the reaction pathway and intermediates produced in the degradation of PNG can be different based on the type of process, the catalyst used, and the degradation mechanism. Also, various intermediate materials have been reported in the photocatalytic process with different catalysts. Studies such as Berkani and coworkers [7], Chavoshan and coworkers [63], and Baladi and coworkers [64] are among the studies that reported intermediate substances produced during the degradation of PNG.

Lastly, Table 7 presents several studies involving the application of different AOPs processes to the degradation of PNG from solution media.
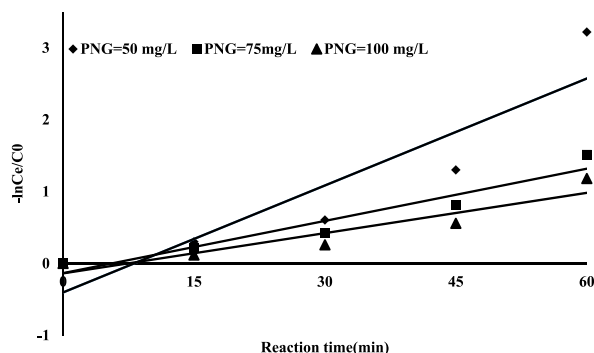
Fig. 11. The kinetics for the degradation of PNG in PCP (pH = 6.5, RT = 59.1 min, PNG concentration = 50,75, and 100 mg/L, and catalyst dose = 18.5 mg/L).

Table 6
The kinetic constants for the degradation of PNG over PCP.

PNG Concentration (mg/L)	$K \times 10^{-2}(min^{-1})$	R^2
50	4.9	0.83
75	2.4	0.92
100	1.8	0.98
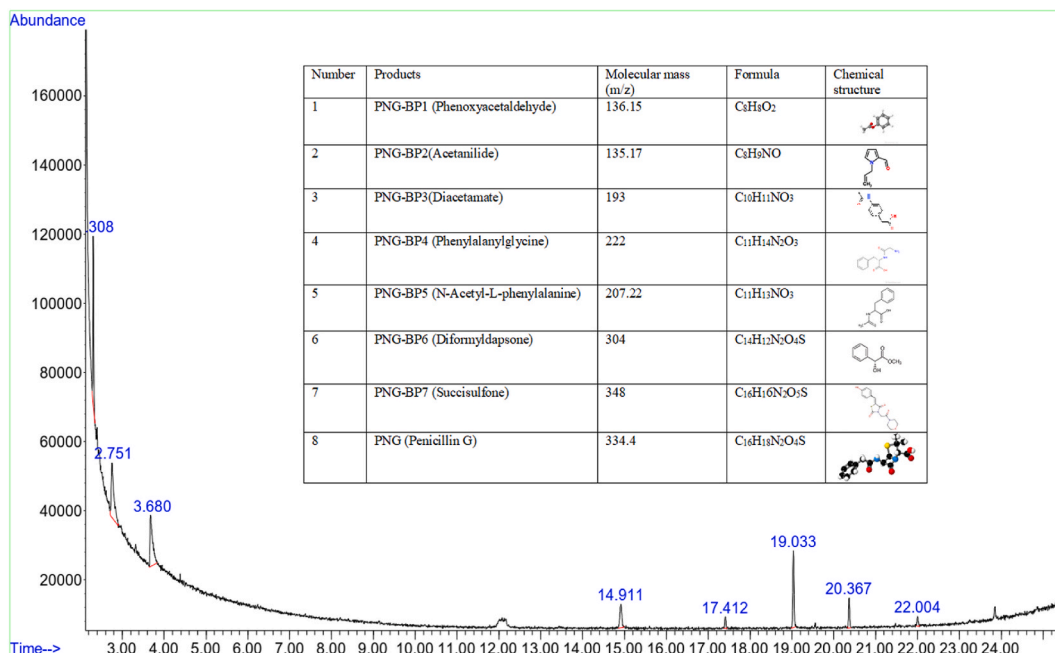
Fig. 12. The analysis of the produced intermediates during PNG degradation via GC–MS (pH = 6.5, RT = 59.1 min, PNG concentration = 50 mg/L, and catalyst dose = 18.5 mg/L).
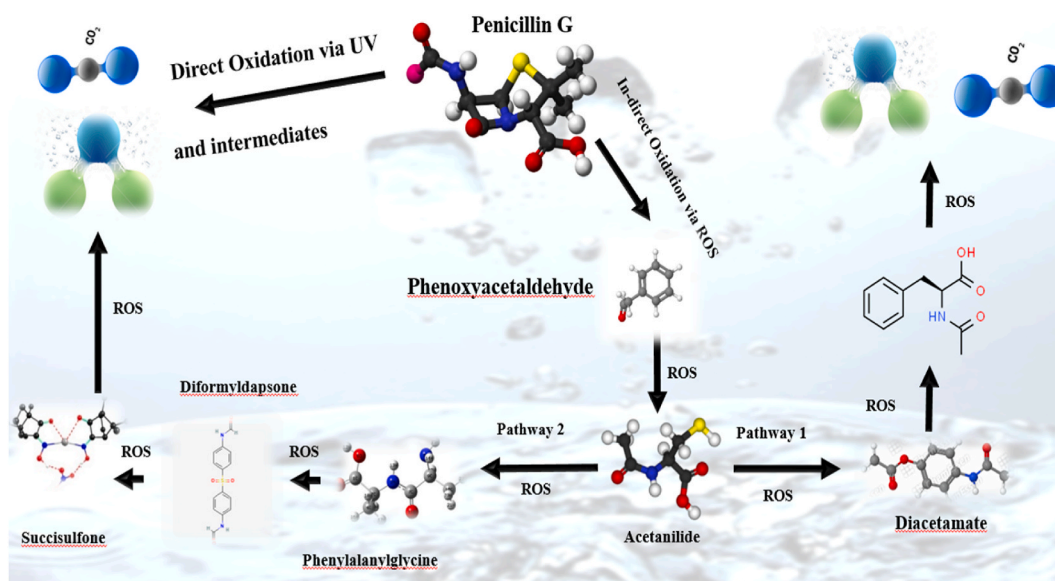
Fig. 13. Proposed degradation pathway of PNG via PCP in optimum condition (pH = 6.5, RT = 59.1 min, PNG concentration = 50 mg/L, and catalyst dose = 18.5 mg/L).

Table 7

Different AOPs studies in PNG degradation.

AOPs process	Results	Ref
$CoFe_2O_4$@CuS nanocomposite Synthesized and photocatalytic degradation of PG	Nanocomposite images obtained by SEM and TEM indicate that its size is less than 100 nm. Photocatalytic degradation of PG resulted in the maximum degradation of PG of 70.7% (pH = 5, nanocomposite dose of 0.2 g/L, PG concentration of 10 mg/L, and contact time of 120 min). Moreover, the photocatalytic reaction exhibited a pseudo-first-order kinetic behavior. Further, no significant decrease in catalyst efficiency was observed after five consecutive runs.	Kamranifar [1]
MMO-Ti/RuO_2IrO_2 anode made and Photoelectrolysis process to PG removal	As a result of photo-electrolysis, the toxicity and antibiotic effect on urine of the bacteria were reduced.	Gonzaga [65]
Fenton-like degradation of penicillin G	A Fenton-like reaction was found to degrade Penicillin G depending on pH, $FeSO_4$ and CaO_2.	Nisapai [66]
Heat-activated/PMS degradation of PNG in solutions	At pH = 5, the maximum removal rate of PNG was obtained and the decomposition of PNG was enhanced by increasing SPS doses from 0.05 to 0.5 mM.	Norzaee [67]
Photocatalytic degradation of Penicillin G (PG)	PG can be completely degraded by PPS at 500 mg L^{-1}. Study results validated the safety and efficiency of the implemented system via Bacillus subtilis, which has demonstrated significant activity. It is highly efficient, low cost, and provides facilities benefits.	Berkani [7]
Synthesis and Characterizations of rGO/Fe^0/Fe_3O_4/TiO_2 Nanocomposite and Optimization of Photocatalytic Process in the Degradation of Penicillin G	The quadratic model of optimization is based on adjusted R^2(0.99), and predicated R^2(0.97) suggested. According to the ANOVA test, the model was significant (F-Value = 162.95, P-Value = 0.0001). The optimum condition of PCP obtained at pH = 6.5, catalyst dose = 18.5 mg/L, reaction time = 59.1 min, and PNG concentration = 52 mg/L (efficiency = 96%). The COD and TOC decrease were 78, and 65%. The photolysis and adsorption mechanism as a single mechanism had lower performance in PNG degradation. BQ had the greatest effect on reducing the efficiency of the process as a radical scavenger. The $^\circ OH$, h^+ and $O_2^{\bullet-}$ were the main ROS in PNG removal. Phenoxyacetaldehyde, Acetanilide, Diacetamate, Phenylalanylglycine, N-Acetyl-L-phenylalanine, Diformyldapsone, and Succisulfone were the main intermediates in PNG degradation.	This study

4. Study limitation

Advanced oxidation processes, including photocatalytic processes, have been investigated over the past few decades, but unfortunately, many of them remain at the laboratory scale. Application on a real scale depends on conducting more extensive studies and also investigating the influencing factors on the treatment process. The main drawback of the photocatalytic process is the cost of the process and its efficiency in real media like industrial wastewater. The presence of interfering factors in wastewater, including other organic substances (as a scavenger), heavy metal ions, and interfering ions are among the factors that limit the application of this process. It is recommended to be used in the real scale, reaction reactor design, the catalyst used (with determining its complete characteristics), environmental influencing factors, etc. should be carefully investigated.

5. Conclusion

This research work studied the synthesized rGO/Fe^0/Fe_3O_4/TiO_2 and optimization of PCP to PNG degradation in aqueous media. In the optimum condition of PCP, supplementary studies were done. Briefly, rGO/Fe^0/Fe_3O_4/TiO_2 nanocomposite was successfully synthesized according to Hummer's, and straightforward sol-gel method. The FESEM, EDX, TEM, FT-IR, XRD, BET, UV spectra, and VSM analysis were applied to determine the catalyst properties. The results of the analysis revealed that the nanocomposite was well synthesized and had superior properties for use in the PCP to organic pollutant degradation. PNG can be detected at very low concentrations using a LOD of 0.001–0.03 mg/L. As an added benefit, the synthesized rGO/Fe^0/Fe_3O_4/TiO_2 nanocomposite is magnetically separable, leading to further degradation along with recyclability of up to five times. The pH, dose of the nanocomposite, and initial concentration of PNG. And reaction time optimized via CCD. The quadratic model of optimization is based on adjusted R^2(0.99), and predicated R^2(0.97) suggested. According to the ANOVA test, the model was significant (F-Value = 162.95, P-Value = 0.0001). The optimum condition of PCP obtained at pH = 6.5, catalyst dose = 18.5 mg/L, reaction time = 59.1 min, and PNG concentration = 52 mg/L (efficiency = 96%). The COD and TOC decrease were 78, and 65%. The photolysis and adsorption mechanism as a single mechanism had lower performance in PNG degradation. BQ had the greatest effect on reducing the efficiency of the process as a radical scavenger. The ROSs ($^\circ OH$, h^+, and $O_2^{\bullet-}$) were the main space in PNG decomposition. Phenoxyacetaldehyde, Acetanilide, Diacetamate, Phenylalanylglycine, N-Acetyl-L-phenylalanine, Diformyldapsone, and Succisulfone were the main intermediates in PNG degradation. This study was done on a laboratory scale and synthetic samples containing PNG. To properly judge the use of the photocatalytic process as well as the synthesized catalyst on a real scale, it is recommended that additional studies be carried out. These studies include surveying the performance of the process with real wastewater containing antibiotics, especially PNG, determining the toxicity of the effluent from the process, examining the economic aspect of the process, etc. By completing these studies, it is possible to decide with certainty regarding the use of this process practical application.

Declarations

Author contribution statement

Jamal Mehralipour: conceived and designed the experiments, analyzed and interpreted the data, materials, contributed reagents, materials, analysis tools or data, wrote the paper.

Susan Bagheri: performed the experiments, materials, contributed reagents, materials, wrote the paper.

Mitra Gholami: conceived and designed the experiments, analyzed and interpreted the data, wrote the paper.

Data availability statement

Data will be made available on request.

Declaration of competing interest

The authors declare that they have no known competing financial interests or personal relationships that could have appeared to influence the work reported in this paper.

Acknowledgements

References

[1] M. Kamranifar, A. Allahresani, A. Naghizadeh, Synthesis and characterizations of a novel CoFe2O4@ CuS magnetic nanocomposite and investigation of its efficiency for photocatalytic degradation of penicillin G antibiotic in simulated wastewater, J. Hazard Mater. 366 (2019) 545–555.

[2] N.A. Khan, S. Ahmed, I.H. Farooqi, I. Ali, V. Vambol, F. Changani, M. Yousefi, S. Vambol, S.U. Khan, A.H. Khan, Occurrence, sources and conventional treatment techniques for various antibiotics present in hospital wastewaters: a critical review, TrAC, Trends Anal. Chem. 129 (2020), 115921.

[3] A. Nasiri, M. Malakootian, M.A. Shiri, G. Yazdanpanah, M. Nozari, CoFe2O4@ methylcellulose synthesized as a new magnetic nanocomposite to tetracycline adsorption: modeling, analysis, and optimization by response surface methodology, J. Polym. Res. 28 (2021) 192.

[4] N.A. Khan, S.U. Khan, S. Ahmed, I.H. Farooqi, M. Yousefi, A.A. Mohammadi, F. Changani, Recent trends in disposal and treatment technologies of emerging-pollutants-A critical review, TrAC, Trends Anal. Chem. 122 (2020), 115921.

[5] M. Alsubih, R. El Morabet, R.A. Khan, N.A. Khan, A.R. Khan, S. Khan, N. Mushtaque, A. Hussain, M. Yousefi, Performance evaluation of constructed wetland for removal of pharmaceutical compounds from hospital wastewater: seasonal perspective, Arab. J. Chem. 15 (2022), 104344.

[6] F. Varanda, M.J. Pratas de Melo, A.I. Caco, R. Dohrn, F.A. Makrydaki, E. Voutsas, D. Tassios, I.M. Marrucho, Solubility of antibiotics in different solvents. 1. Hydrochloride forms of tetracycline, moxifloxacin, and ciprofloxacin, Ind. Eng. Chem. Res. 45 (2006) 6368–6374.

[7] M. Berkani, A. Smaali, Y. Kadmi, F. Almomani, Y. Vasseghian, N. Lakhdari, M. Alyane, Photocatalytic degradation of Penicillin G in aqueous solutions: kinetic, degradation pathway, and microbioassays assessment, J. Hazard Mater. 421 (2022), 126719.

[8] H. Sharifpour, N. Javid, M. Malakootian, Investigation of single-walled carbon nanotubes in removal of Penicillin G (Benzyl penicillin sodium) from aqueous environments, Desalination Water Treat. 124 (2018) 248–255.

[9] S. Aghagani, H. Baseri, Production of magnetic biochar from the Hazelnut shell and magnetite particles for adsorption of Penicillin-G from the contaminated water, Urban Water J. (2022) 1–11.

[10] B. Erim, Z. Ciğeroğlu, S. Şahin, Y. Vasseghian, Photocatalytic degradation of cefixime in aqueous solutions using functionalized SWCNT/ZnO/Fe3O4 under UV-A irradiation, Chemosphere 291 (2022), 132929.

[11] K.M.S. Ana, J. Madriaga, M.P. Espino, β-Lactam antibiotics and antibiotic resistance in Asian lakes and rivers: an overview of contamination, sources and detection methods, Environ. Pollut. 275 (2021), 116624.

[12] A. Ghamkhari, L. Mohamadi, S. Kazemzadeh, M.N. Zafar, A. Rahdar, R. Khaksefidi, Synthesis and characterization of poly(styrene-block-acrylic acid) diblock copolymer modified magnetite nanocomposite for efficient removal of penicillin G, Compos. B Eng. 182 (2020), 107643.

[13] J. Zhang, Z. Xiong, J. Wei, Y. Song, Y. Ren, D. Xu, B. Lai, Catalytic ozonation of penicillin G using cerium-loaded natural zeolite (CZ): efficacy, mechanisms, pathways and toxicity assessment, Chem. Eng. J. 383 (2020), 123144.

[14] Y. De Luna, N. Bensalah, Review on the electrochemical oxidation of endocrine-disrupting chemicals using BDD anodes, Curr. Opin. Electrochem. 32 (2022), 100900.

[15] E. Brillas, Progress of homogeneous and heterogeneous electro-Fenton treatments of antibiotics in synthetic and real wastewaters. A critical review on the period 2017–2021, Sci. Total Environ. 819 (2022), 153102.

[16] W. Zheng, X. Wen, B. Zhang, Y. Qiu, Selective effect and elimination of antibiotics in membrane bioreactor of urban wastewater treatment plant, Sci. Total Environ. 646 (2019) 1293–1303.

[17] X. Liu, F. Li, Y. Liu, P. Li, L. Chen, B. Li, T. Qian, W. Liu, Degradation of diclofenac in a photosensitization-like photocatalysis process using palladium quantum dots deposited graphite carbon nitride under solar light, J. Environ. Chem. Eng. 10 (2022), 107545.

[18] Y. Jiang, Z. Wang, J. Huang, F. Yan, Y. Du, C. He, Y. Liu, G. Yao, B. Lai, A singlet oxygen dominated process through photocatalysis of CuS-modified MIL-101 (Fe) assisted by peroxymonosulfate for efficient water disinfection, Chem. Eng. J. 439 (2022), 135788.

[19] I. Abdouli, F. Dappozze, M. Eternot, N. Essayem, C. Guillard, Hydrothermal process assisted by photocatalysis: towards a novel hybrid mechanism driven glucose valorization to levulinic acid, ethylene and hydrogen, Appl. Catal. B Environ. 305 (2022), 121051.

[20] Y. Wang, S. Wang, Y. Wu, Z. Wang, H. Zhang, Z. Cao, J. He, W. Li, Z. Yang, L. Zheng, D. Feng, P. Pan, J. Bi, H. Li, J. Zhao, K. Zhang, A α-Fe2O3/rGO magnetic photocatalyst: enhanced photocatalytic performance regulated by magnetic field, J. Alloys Compd. 851 (2021), 156733.

[21] N. Olama, M. Dehghani, M. Malakootian, The removal of amoxicillin from aquatic solutions using the TiO 2/UV-C nanophotocatalytic method doped with trivalent iron, Appl. Water Sci. 8 (2018) 1–12.

[22] A. Kumar, P. Choudhary, A. Kumar, P.H. Camargo, V. Krishnan, Recent advances in plasmonic photocatalysis based on TiO2 and noble metal nanoparticles for energy conversion, environmental remediation, and organic synthesis, Small 18 (2022), 2101638.

[23] Z. Braiek, J.B. Naceur, F. Jrad, I.B. Assaker, R. Chtourou, Novel synthesis of graphene oxide/In2S3/TiO2 NRs heterojunction photoanode for enhanced photoelectrochemical (PEC) performance, Int. J. Hydrogen Energy 47 (2022) 3655–3666.

[24] S. Bagheri, A. Esrafili, M. Kermani, J. Mehralipour, M. Gholami, Performance evaluation of a novel rGO-Fe0/Fe3O4-PEI nanocomposite for lead and cadmium removal from aqueous solutions, J. Mol. Liq. 320 (2020) 114422.

[25] F.A. Tapouk, R. Nabizadeh, S. Nasseri, A. Mesdaghinia, H. Khorsandi, M. Yousefi, M. Alimohammadi, M. Khoobi, Embedding of L–Arginine into graphene oxide (GO) for endotoxin removal from water: modeling and optimization approach, Colloids Surf. A Physicochem. Eng. Asp. 607 (2020), 125491.

[26] M. Nozari, M. Malakootian, N.J.H. Fard, H. Mahmoudi-Moghaddam, Synthesis of Fe3O4@ PAC as a magnetic nano-composite for adsorption of dibutyl phthalate from the aqueous medium: modeling, analysis and optimization using the response surface methodology, Surface. Interfac. 31 (2022), 101981.

[27] S. Xu, Y. Zhang, S. Pan, H. Ding, G. Li, Recyclable magnetic photocatalysts of Fe2+/TiO2 hierarchical architecture with effective removal of Cr (VI) under UV light from water, J. Hazard Mater. 196 (2011) 29–35.

[28] Z.-H. Diao, X.-R. Xu, D. Jiang, J.-J. Liu, L.-J. Kong, G. Li, L.-Z. Zuo, Q.-H. Wu, Simultaneous photocatalytic Cr(VI) reduction and ciprofloxacin oxidation over TiO2/Fe0 composite under aerobic conditions: performance, durability, pathway and mechanism, Chem. Eng. J. 315 (2017) 167–176.

[29] S. Bibi, A. Ahmad, M.A.R. Anjum, A. Haleem, M. Siddiq, S.S. Shah, A.A. Kahtani, Photocatalytic degradation of malachite green and methylene blue over reduced graphene oxide (rGO) based metal oxides (rGO-Fe3O4/TiO2) nanocomposite under UV-visible light irradiation, J. Environ. Chem. Eng. 9 (2021), 105580.

[30] A. Motla, A. Sharma Kaushik, M. Tomar, V. Gupta, Effect of sonication of GO in acetone for the fabrication of RGO powder and thin film, in: Advanced Functional Materials and Devices, Springer, 2022, pp. 97–103.

[31] N.K. Cakmak, Z. Said, L.S. Sundar, Z.M. Ali, A.K. Tiwari, Preparation, characterization, stability, and thermal conductivity of rGO-Fe3O4-TiO2 hybrid nanofluid: an experimental study, Powder Technol. 372 (2020) 235–245.

[32] S.P. Kim, M.Y. Choi, H.C. Choi, Photocatalytic activity of SnO2 nanoparticles in methylene blue degradation, Mater. Res. Bull. 74 (2016) 85–89.

[33] M.J. Haque, M.M. Bellah, M.R. Hassan, S. Rahman, Synthesis of ZnO nanoparticles by two different methods & comparison of their structural, antibacterial, photocatalytic and optical properties, Nano Express 1 (2020), 010007.

[34] M. Yousefi, M. Gholami, V. Oskoei, A.A. Mohammadi, M. Baziar, A. Esrafili, Comparison of LSSVM and RSM in simulating the removal of ciprofloxacin from aqueous solutions using magnetization of functionalized multi-walled carbon nanotubes: process optimization using GA and RSM techniques, J. Environ. Chem. Eng. 9 (2021), 105677.

[35] S. Khoramipour, J. Mehralipour, M. Hosseini, Optimisation of ultrasonic-electrocoagulation process efficiency in the landfill leachate treatment: a novel advanced oxidation process, Int. J. Environ. Anal. Chem. (2021) 1–19.

[36] A.D. Eaton, L.S. Clesceri, A.E. Greenberg, Standard Methods for the Examination of Water and Wastewater, American Public Health Association, Washington, DC, 2005, pp. 20001–23710.

[37] P. Benjwal, M. Kumar, P. Chamoli, K.K. Kar, Enhanced photocatalytic degradation of methylene blue and adsorption of arsenic (iii) by reduced graphene oxide (rGO)–metal oxide (TiO 2/Fe 3 O 4) based nanocomposites, RSC Adv. 5 (2015) 73249–73260.

[38] M. Pudukudy, Q. Jia, Y. Dong, Z. Yue, S. Shan, Magnetically separable and reusable rGO/Fe 3 O 4 nanocomposites for the selective liquid phase oxidation of cyclohexene to 1, 2-cyclohexane diol, RSC Adv. 9 (2019) 32517–32534.

[39] Y. Yu, L. Yan, J. Cheng, C. Jing, Mechanistic insights into TiO2 thickness in Fe3O4@ TiO2-GO composites for enrofloxacin photodegradation, Chem. Eng. J. 325 (2017) 647–654.

[40] K.D.V. Nguyen, K.D.N. Vo, Magnetite nanoparticles-TiO 2 nanoparticles-graphene oxide nanocomposite: synthesis, characterization and photocatalytic degradation for Rhodamine-B dye, AIMS Mater. Sci. 7 (2020) 288–301.

[41] M.A. Baghchesara, H.R. Azimi, A. Ghorban Shiravizadeh, M. Asri Mat Teridi, R. Yousefi, Improving the intrinsic properties of rGO sheets by S-doping and the effects of rGO improvements on the photocatalytic performance of Cu3Se2/rGO nanocomposites, Appl. Surf. Sci. 466 (2019) 401–410.

[42] P.K. Boruah, M.R. Das, Dual responsive magnetic Fe3O4-TiO2/graphene nanocomposite as an artificial nanozyme for the colorimetric detection and photodegradation of pesticide in an aqueous medium, J. Hazard Mater. 385 (2020), 121516.

[43] H. Fan, G. Yi, X. Zhang, B. Xing, C. Zhang, L. Chen, Y. Zhang, Facile synthesis of uniformly loaded Fe3O4–TiO2/RGO ternary hybrids for enhanced photocatalytic activities, Opt. Mater. 111 (2021), 110582.

[44] Z.-Q. Li, H.-L. Wang, L.-Y. Zi, J.-J. Zhang, Y.-S. Zhang, Preparation and photocatalytic performance of magnetic TiO2–Fe3O4/graphene (RGO) composites under VIS-light irradiation, Ceram. Int. 41 (2015) 10634–10643.

[45] G.I. Danmaliki, T.A. Saleh, A.A. Shamsuddeen, Response surface methodology optimization of adsorptive desulfurization on nickel/activated carbon, Chem. Eng. J. 313 (2017) 993–1003.

[46] A. Arslan, E. Topkaya, D. Bingöl, S. Veli, Removal of anionic surfactant sodium dodecyl sulfate from aqueous solutions by O3/UV/H2O2 advanced oxidation process: process optimization with response surface methodology approach, Sustain. Environ. Res. 28 (2018) 65–71.

[47] M. Iqbal, N. Iqbal, I.A. Bhatti, N. Ahmad, M. Zahid, Response surface methodology application in optimization of cadmium adsorption by shoe waste: a good option of waste mitigation by waste, Ecol. Eng. 88 (2016) 265–275.

[48] N.A.A. Fatah, S. Triwahyono, A.A. Jalil, N. Salamun, C.R. Mamat, Z.A. Majid, n-Heptane isomerization over molybdenum supported on bicontinuous concentric lamellar silica KCC-1: influence of phosphorus and optimization using response surface methodology (RSM), Chem. Eng. J. 314 (2017) 650–659.

[49] J. Wang, R. Zhuan, Degradation of antibiotics by advanced oxidation processes: an overview, Sci. Total Environ. 701 (2020), 135023.

[50] S. Chavoshan, M. Khodadadi, N. Nasseh, Photocatalytic degradation of penicillin G from simulated wastewater using the UV/ZnO process: isotherm and kinetic study, J. Environ. Heal. Sci. Eng. 18 (2020) 107–117.

[51] H.R. Pouretedal, M.A. Hasanali, Photocatalytic degradation of some β-lactam antibiotics in aqueous suspension of ZnS nanoparticles, Desalination Water Treat. 51 (2013) 2617–2623.

[52] T.J. Al-Musawi, P. Rajiv, N. Mengelizadeh, F. Sadat Arghavan, D. Balarak, Photocatalytic efficiency of CuNiFe2O4 nanoparticles loaded on multi-walled carbon nanotubes as a novel photocatalyst for ampicillin degradation, J. Mol. Liq. 337 (2021), 116470.

[53] A. Rathi, S. Basu, S. Barman, Efficient eradication of antibiotic and dye by C-dots@zeolite nanocomposites: performance evaluation, and degraded products analysis, Chemosphere 298 (2022), 134260.

[54] B.M. Pirzada, Pushpendra, R.K. Kunchala, B.S. Naidu, Synthesis of LaFeO3/Ag2CO3 nanocomposites for photocatalytic degradation of rhodamine B and p-chlorophenol under natural sunlight, ACS Omega 4 (2019) 2618–2629.

[55] Y. Yu, D. Chen, W. Xu, J. Fang, J. Sun, Z. Liu, Y. Chen, Y. Liang, Z. Fang, Synergistic adsorption-photocatalytic degradation of different antibiotics in seawater by a porous g-C3N4/calcined-LDH and its application in synthetic mariculture wastewater, J. Hazard Mater. 416 (2021), 126183.

[56] S. Song, B. Cheng, N. Wu, A. Meng, S. Cao, J. Yu, Structure effect of graphene on the photocatalytic performance of plasmonic Ag/Ag2CO3-rGO for photocatalytic elimination of pollutants, Appl. Catal. B Environ. 181 (2016) 71–78.

[57] M.A. Zazouli, F. Ghanbari, M. Yousefi, S. Madihi-Bidgoli, Photocatalytic degradation of food dye by Fe3O4–TiO2 nanoparticles in presence of peroxymonosulfate: the effect of UV sources, J. Environ. Chem. Eng. 5 (2017) 2459–2468.

[58] T.J. Al-Musawi, P. Rajiv, N. Mengelizadeh, F.S. Arghavan, D. Balarak, Photocatalytic efficiency of CuNiFe2O4 nanoparticles loaded on multi-walled carbon nanotubes as a novel photocatalyst for ampicillin degradation, J. Mol. Liq. 337 (2021), 116470.

[59] S. Banerjee, P. Benjwal, M. Singh, K.K. Kar, Graphene oxide (rGO)-metal oxide (TiO2/Fe3O4) based nanocomposites for the removal of methylene blue, Appl. Surf. Sci. 439 (2018) 560–568.

[60] K. Saravanakumar, C.M. Park, Rational design of a novel LaFeO3/g-C3N4/BiFeO3 double Z-scheme structure: photocatalytic performance for antibiotic degradation and mechanistic insight, Chem. Eng. J. 423 (2021), 130076.

[61] L.L. Albornoz, S.W. da Silva, J.P. Bortolozzi, E.D. Banús, P. Brussino, M.A. Ulla, A.M. Bernardes, Degradation and mineralization of erythromycin by heterogeneous photocatalysis using SnO2-doped TiO2 structured catalysts: activity and stability, Chemosphere 268 (2021), 128858.

[62] C. Sekaran, D. Vishnu, B. Dhandapani, T. Alagesan, G. Balaji, Facile synthesis of zinc oxide nanoparticles using glycerol as cross-linker and the kinetic studies for the photocatalytic degradation of acid blue 113 dye, Resul. Chem. 4 (2022), 100377.

[63] S. Chavoshan, M. Khodadadi, N. Nasseh, Photocatalytic degradation of penicillin G from simulated wastewater using the UV/ZnO process: isotherm and kinetic study, J. Environ. Heal. Sci. Eng. 18 (2020) 107–117.

[64] E. Baladi, F. Davar, A. Hojjati-Najafabadi, Synthesis and characterization of g–C3N4–CoFe2O4–ZnO magnetic nanocomposites for enhancing photocatalytic activity with visible light for degradation of penicillin G antibiotic, Environ. Res. 215 (2022), 114270.

[65] I.M. Gonzaga, A. Moratalla, K.I. Eguiluz, G.R. Salazar-Banda, P. Cañizares, M.A. Rodrigo, C. Saez, Outstanding performance of the microwave-made MMO-Ti/RuO2IrO2 anode on the removal of antimicrobial activity of Penicillin G by photoelectrolysis, Chem. Eng. J. 420 (2021), 129999.

[66] W. Nisapai, A. Paikamnam, P. Sriprom, W. Sangsida, S. Neramittagapong, S. Theerakulpisut, A. Neramittagapong, Influencing factors on degradation of penicillin G by fenton-like reaction, Thai Environ. Eng. J. 35 (2021) 13–19.

[67] S. Norzaee, M. Taghavi, B. Djahed, F. Kord Mostafapour, Degradation of Penicillin G by heat activated persulfate in aqueous solution, J. Environ. Manag. 215 (2018) 316–323.